QUANTITATIVE ANALYSIS OF MELT INCLUSIONS IN EXTRATERRESTRIAL SAMPLES USING NANO-SCALE X-RAY COMPUTED TOMOGRAPHY P. Wu[1], K. Dayton[1], and E. Gazel[1], [1]Department of Earth and Atmospheric Sciences, Cornell University (pw443@cornell.edu, kad283@cornell.edu, egazel@cornell.edu)

Introduction: X-ray computed tomography (XCT) is a non-invasive/destructive, 3D imaging technique that enables the visualization of internal features within non-transparent materials. It has been widely used in geoscience research over the past two decades due to its ability to quickly analyze and interpret maps of materials with different densities and compositions [1-3]. XCT is particularly useful for analyzing rare extraterrestrial samples (i.e., meteorites or returned specimens), where sample preservation is a priority [4-6]. For instance, the non-destructive nature of XCT makes it a key method for characterizing and distributing returned Mars samples in the context of both life detection and planetary protection [7, 8]. Initial results from XCT analysis can then be used to inform decisions about sub-sampling, efficient analytical work, and curation [7, 8].

Previous studies demonstrated the usefulness of XCT for observations of rare extraterrestrial materials, through the provision of bulk volumetric and textural phase information. To further investigate the record of melting processes and evolution conditions of meteorites and returned samples, it is critical to determine their potential parental magma compositions. Olivine-hosted melt inclusions (droplets of magmatic liquid trapped inside growing crystals) are used to estimate the parental magma compositions of cumulate rocks, for which bulk chemistry cannot be used to define their magmatic source compositions [9-15].

Here, we demonstrate the capabilities and future perspectives of applying XCT on the study of melt inclusions hosted in extraterrestrial materials. For the first time, we use X-ray nano-CT (nanoscale XCT) in combination with Fourier-transform infrared (FTIR) and Raman spectroscopy to identify and reconstruct 3D phase distributions of olivine-hosted melt inclusions in an extraterrestrial sample, Northwest Africa (NWA) 2737 martian meteorite. This study develops a benchmarking protocol to locate melt inclusion sites in a bulk meteorite scan and assesses the reliability of 2D phase abundance estimations.

Methods: NWA 2737 is characterized by a cumulate texture and consists of over 85% of anhedral to subhedral olivine, 4-9% pyroxene (augite, pigeonite, and orthopyroxene), 3-5% chromite, and ~3% of other minerals including feldspathic and granitic glass, kaersutite amphibole, ilmenite, apatite, rutile, and Fe-sulfide [12, 16, 17]. Crystals nucleated after the silicate melts were trapped, creating multiphase melt inclusions. Phases identified in NWA 2737 olivine-hosted melt inclusions include low-Ca pyroxene, kaersutitic amphibole, augite, apatite, chromite, sulfide, alkali-rich glass, and some Ti-biotite [12]. Most olivine crystals are dark green-brown stained with dispersed metallic nanoparticles (high abundance of Fe^{3+}) that resulted from a shock event [16, 18, 19] making it challenging to identify inclusions by traditional optical methods.

We used a Zeiss Xradia 520 Versa nano-CT (Biotechnology Resource Center, Cornell University, Ithaca, NY) which can achieve voxel sizes between 150 nm and 50 μm and accommodate specimens as large as 30 cm in diameter to collect scans with different resolutions (0.75 μm -12.43 μm/pixel) and laser powers (100 kV-160 kV). We applied nano-CT scans on both a bulk chip (1.12 cm x 1.46 cm) of NWA 2737 and the olivine-hosted melt inclusions within the chip.

To account for instrumental shifts and create a standardized mineral database that can be applied in future studies, we selected two standards as reference materials: one high-density endmember (spinel) and one mid-density endmember (olivine). Using the Fiji software, we plotted gray value profile lines across the bulk sample and used the averaged gray values of the spinel and olivine endmembers as reference points. These gray values were then used to calculate a gray value database for other commonly observed phases in martian meteorites. For the best tradeoff between achieving enough phase contrast while minimizing instrumental artifacts, we tested three different laser powers (100 kV, 130 kV, and 160 kV) at a resolution of 7.91 μm/pixel.

Results: Fig.1 shows linear gray value profiles from point A' to B' and from point C' to D'. A clear change in gray value is shown when phases with higher density contrast are present (i.e., spinel and glass). Phases with similar gray values (i.e., olivine and pyroxene) are also distinguishable after the cupping artifact is reduced. We then used the averaged gray value of olivine extracted from the gray value profile lines as the mid-density endmember for the gray value database calibration. Using the FTIR map as a reference, we were able to separate 4 phases in the bulk piece nano-CT slices (7.91 μm/voxel) (Fig. 1): olivine, pyroxene, chromite, and glass. 84% of olivine, 9.7% of pyroxene, 3.8% of chromite, and 2.6% of glass were calculated based on the average number of segmented voxels.

Multi-phase melt inclusions were found near the center of olivine grains, close to the edges of the grains, and within the fractures. Similar to the bulk scan, 4 phases within the melt inclusions, including olivine,

pyroxene, chromite, and glass, were able to be distinguished in the nano-CT scan (1.54 μm/pixel). Again, we calculated the averaged gray value of olivine by drawing a gray value profile line and used the averaged olivine gray value as the mid-density endmember for the gray value database calibration. 46% of glass, 49% of pyroxene, and 3.6% of chromite were calculated based on the average number of segmented voxels.

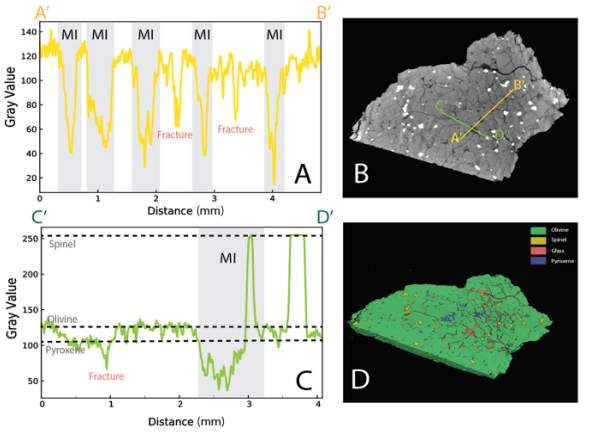

Figure 1. Linear gray value profiles are plotted across line A'B' (A) and line C'D' (C). 5 melt inclusions are identified along A'B' (A) and same melt inclusion sites can be identified after 3D phase segmentation using Avizo (D). Olivine and pyroxene are distinguishable as shown in C. Fractures/melt veins are shown as sudden dips in gray values.

Discussion: Many studies on the bulk composition of melt inclusions found in martian meteorites have relied on 2-D area distributions of phases to estimate the composition of the parental magma. However, this approach can potentially lead to inaccuracies in the calculated compositions. For instance, previous compositions for the chassignite parental magma, as found in Chassigny and NWA 2737, were calculated using a combination of mineral chemistry determined through electron microprobe analysis and phase proportions estimated using scanning electron microscope (SEM) with backscattered electron (BSE) imaging [12, 20, 21]. These compositions may be subject to revision following further experiments [15].

Controversy exists regarding the proposed compositions for the chassignite parental magma, as experiments and models utilizing these compositions under various water (dry to 2 wt.%) and pressure conditions (up to 15.7 kbar) have been unable to reproduce the commonly found hydrous phase, kaersutite, in NWA 2737 melt inclusions [10, 15]. Crystallization paths compared with *in situ* martian compositions also suggested that the parental liquid to chassignites could have gone through assimilation and could be more Mg- and Al-rich than previously proposed [9, 22].

Potential errors when estimating the abundance of phases in melt inclusions using their 2-D visible portion can occur when determining if an inclusion is representative or simply an off-center cut, and when deciding whether a phase is primary or secondary. A 3-D representation of phase distributions can significantly improve the accuracy of phase portion calculation and more accurately determine the bulk composition of these melt inclusions.

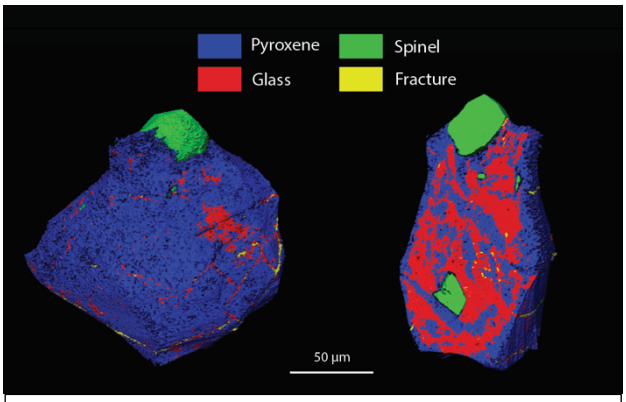

Figure 2. High-resolution (1.54 μm/pixel) scan of a representative crystallized melt inclusion in the bulk piece.

Acknowledgments: Imaging data was acquired through the Cornell Institute of Biotechnology's Imaging Facility, with NIH 1S10OD012287 funding for the Zeiss-Xradia Versa 520 X-ray microscope. This project was supported by NASA award 20-SSW20-0066.

References: [1] Cnudde, V. and M.N. Boone (2013) *Earth-Sci Rev. 123* 1. [2] Zhang, P. et al (2019) *Micron. 124* 102702. [3] Ketcham, R.A. and W.D. Carlson (2001) *Comput Geosci. 27* 381. [4] Hanna, R.D. and R.A. Ketcham (2017) *Geoch. 77* 547. [5] Needham, A.W., et al. (2013) *Meteorit. Planet. Sci. 116* 96. [6] Ebel, D.S. and M.L. Rivers (2007) *Meteorit. Planet. Sci. 42* 1627. [7] Welzenbach, L., et al. (2018) *EPSC* 1182. [8] Kminek, G., et al. (2014) *Life Sci. in Spa. Research. 2* 1. [9] Ostwald, A., et al. (2022) *EPSL. 585* 117514. [10] Nekvasil, H., et al. (2007) *Meteorit. Planet. Sci. 42* 979. [11] Johnson, M.C., et al. (1991) *Geochim. Cosmochim. Acta. 55* 349. [12] He, Q., et al. (2013) *Meteorit. Planet. Sci. 48* 474. [13] Goodrich, C.A., et al. (2013) *Meteorit. Planet. Sci. 48* 2371. [14] Filiberto, J. (2017) *Chem. Geol. 466* 1. [15] Filiberto, J. (2008) *Geochim. Cosmochim. Acta. 72* 690. [16] Treiman, A.H., et al. (2007) *JGR: Planets. 112* E4. [17] Beck, P., et al. (2006) *Geochim. Cosmochim. Acta. 70* 2127. [18] Van de Moortèle, B., et al. (2007) *EPSL. 262* 37. [19] Bläß, U.W., et al. (2010) *EPSL 300* 255. [20] Peslier, A.H. (2010) *JVGR. 197* 239. [21] Goodrich, C.A. (2003) *Geochim. Cosmochim. Acta. 67* 3735. [22] Wu, P., et al. (2021) *Meteorit. Planet. Sci. 56* 1328.